Estimating Infrared Radiometric Satellite Sea Surface Temperature Retrieval Cold Biases in the Tropics due to Unscreened Optically Thin Cirrus Clouds

Citation: Marquis, Jared W. et al. "Estimating Infrared Radiometric Satellite Sea Surface Temperature Retrieval Cold Biases in the Tropics Due to Unscreened Optically Thin Cirrus Clouds." Journal of Atmospheric and Oceanic Technology 34, 2 (February 2017): 355–373 © 2017 American Meteorological Society

As Published: http://dx.doi.org/10.1175/JTECH-D-15-0226.1

Publisher: American Meteorological Society

Persistent URL: http://hdl.handle.net/1721.1/111125

Version: Final published version: final published article, as it appeared in a journal, conference proceedings, or other formally published context

Estimating Infrared Radiometric Satellite Sea Surface Temperature Retrieval Cold Biases in the Tropics due to Unscreened Optically Thin Cirrus Clouds

JARED W. MARQUIS

Department of Atmospheric Sciences, University of North Dakota, Grand Forks, North Dakota

ALEC S. BOGDANOFF

Massachusetts Institute of Technology–WHOI Joint Program in Oceanography, Woods Hole, Massachusetts

JAMES R. CAMPBELL, JAMES A. CUMMINGS, AND DOUGLAS L. WESTPHAL

U.S. Naval Research Laboratory, Monterey, California

NATHANIEL J. SMITH AND JIANGLONG ZHANG

Department of Atmospheric Sciences, University of North Dakota, Grand Forks, North Dakota

(Manuscript received 23 October 2015, in final form 9 November 2016)

ABSTRACT

Passive longwave infrared radiometric satellite–based retrievals of sea surface temperature (SST) at instrument nadir are investigated for cold bias caused by unscreened optically thin cirrus (OTC) clouds [cloud optical depth (COD) ≤ 0.3]. Level 2 nonlinear SST (NLSST) retrievals over tropical oceans (30°S–30°N) from Moderate Resolution Imaging Spectroradiometer (MODIS) radiances collected aboard the NASA *Aqua* satellite (*Aqua*-MODIS) are collocated with cloud profiles from the Cloud–Aerosol Lidar with Orthogonal Polarization (CALIOP) instrument. OTC clouds are present in approximately 25% of tropical quality-assured (QA) *Aqua*-MODIS Level 2 data, representing over 99% of all contaminating cirrus found. Cold-biased NLSST (MODIS, AVHRR, and VIIRS) and triple-window (AVHRR and VIIRS only) SST retrievals are modeled based on operational algorithms using radiative transfer model simulations conducted with a hypothetical 1.5-km-thick OTC cloud placed incrementally from 10.0 to 18.0 km above mean sea level for cloud optical depths between 0.0 and 0.3. Corresponding cold bias estimates for each sensor are estimated using relative *Aqua*-MODIS cloud contamination frequencies as a function of cloud-top height and COD (assuming they are consistent across each platform) integrated within each corresponding modeled cold bias matrix. NLSST relative OTC cold biases, for any single observation, range from 0.33° to 0.55°C for the three sensors, with an absolute (bulk mean) bias between 0.09° and 0.14°C. Triple-window retrievals are more resilient, ranging from 0.08° to 0.14°C relative and from 0.02° to 0.04°C absolute. Cold biases are constant across the Pacific and Indian Oceans. Absolute bias is lower over the Atlantic but relative bias is higher, indicating that this issue persists globally.

1. Motivation

Sea surface temperature (SST) measurements are a core input for a host of meteorological and oceanographic modeling systems (e.g., Kelley et al. 2002; Harris and Maturi 2003; Tang et al. 2004; Donlon et al. 2007; Miyazawa et al. 2013). In theory, errors in background model SSTs can be mitigated by assimilating observed values, resulting in increased forecast skill. Tropical cyclone (TC) intensity forecasting, for instance, represents one specific area of significance for SST assimilation. Studies have shown exponential relationships between TC strength and SST using both maximum wind (Demaria and Kaplan 1994) and minimum pressure (Miller 1958) as

---

Corresponding author e-mail: Jared W. Marquis, jared.marquis@und.edu

Publisher's Note: This article was revised on 9 February 2017 to include additional funding information that was missing when originally published.

DOI: 10.1175/JTECH-D-15-0226.1

proxies for intensity. Thus, accurate SSTs are essential for accurate TC prediction. Additionally, El Niño–Southern Oscillation (ENSO) forecasts are highly dependent on SST (Tang et al. 2004). The proper understanding and prediction of the global weather implications of ENSO require correct SST fields at model initialization.

While the spatial and temporal coverage of in situ SST measurements is improving (e.g., Roemmich et al. 2009), high-resolution global daily measurements remain unavailable. Thus, SSTs retrieved from passive radiometric remote sensors aboard Earth-orbiting satellites are the primary source of global estimates. Satellite-borne infrared (IR) radiometers in current use for SST retrievals include the Advanced Very High Resolution Radiometer (AVHRR; Walton 1988), Geostationary Operational Environmental Satellites (GOES; Wu et al. 1999), the Moderate Resolution Imaging Spectroradiometer (MODIS; Brown et al. 1999), and the Visible Infrared Imaging Radiometer Suite (VIIRS; Petrenko et al. 2014). SST retrieval algorithms designed for each sensor are based on the specific IR channels available for each instrument.

Early satellite sensors used only a shortwave IR channel to retrieve SST (e.g., Deschamps and Phulpin 1980; Barton 1995). However, such shortwave channels are highly susceptible to errors associated with solar reflection during daylight hours, traditionally limiting the corresponding SST retrievals to nighttime only. Beginning in 1981 with the launch of the *NOAA-7* satellite, the AVHRR instrument afforded "split window" longwave IR channels at 10.8- and 11.9-μm wavelengths, making daytime SST retrievals more practical (Llewellyn-Jones et al. 1984; McClain et al. 1985; Barton 1995; Davis 2007). Whereas *GOES-12* has also been used for "dual window" SST retrievals during the day using the 11- and 3.9-μm bands, because of the lack of a 12-μm band, solar contamination is a significant determining factor in product fidelity overall (Merchant et al. 2009; Koner et al. 2015).

The longwave IR split-window technique is based upon the assumption that the difference between the SST retrieval and brightness temperatures near 11 μm is proportional to the difference between the SST retrieval and brightness temperatures near 12 μm (Merchant et al. 2009). Building upon the IR split-window technique is the nonlinear SST (NLSST) retrieval technique. While the split-window technique assumes proportionality between the SST and the 11- and 12-μm brightness temperatures is constant, the NLSST assumes this proportionality actually varies as a function of column water vapor (Barton 1995). Unlike the split-window technique, NLSST requires the use of a first guess, or climatological SST. Building on this, the Pathfinder SST retrieval uses coefficients that vary depending on column water vapor: one set for low water vapor and one for low water vapor as determined using the difference in 11- and 12-μm brightness temperatures (Kilpatrick et al. 2001). For moderate integrated column water vapor, interpolation between high and low coefficients is performed.

Triple-window algorithms (e.g., Deschamps and Phulpin 1980) combine the 3.9-μm band with the 11- and 12-μm bands. Since water vapor absorption is significantly lower at 3.9 μm than at 11 and 12 μm, and the Planck function is steeper, the signal-to-noise is higher in the former, and triple-window retrievals are more tolerant of residual cloud contamination. Thus, triple-window SSTs are generally considered to exhibit the highest skill of all current IR retrieval methods despite being used traditionally for only half of the diurnal cycle (e.g., Pichel et al. 2001).

IR radiometers measure column-integrated radiances, and thus the presence of cloud and large aerosol particles negatively impacts their corresponding SST retrievals, which are fundamentally based on the assumption of clear skies. Consequently, SST algorithms are designed to identify and remove cloudy pixels. Operational MODIS SST cloud screening, for instance, is achieved through a series of threshold, spatial homogeneity, and climatology tests (Brown et al. 1999). Despite these efforts, however, residual cloud contamination remains, particularly with respect to optically thin cirrus clouds. Sassen and Cho (1992) define these unique clouds as exhibiting translucence with respect to blue sky above them, as evident to a ground observer. Conversely, a nadir-viewing IR radiometric imager presumably senses the relatively warm ground below, making them difficult to distinguish relative to surrounding clear skies or background surface features in terms of spatial and thermal contrast.

Ackerman et al. (2008) demonstrate how the lower threshold sensitivity of the MODIS cloud product tends to occur very near a cloud optical depth (COD) of 0.30, or the approximate upper threshold of optically thin cirrus (OTC) presence advocated by Sassen and Cho (1992). Similar bias has been identified in the MODIS aerosol product. Toth et al. (2013) report the presence of both cirrus and low-topped near-surface clouds in otherwise quality-assured MODIS aerosol optical depth retrievals. Ground-based solar/near-IR radiometers used by the Aerosol Robotic Network (AERONET) have also been found to exhibit significant OTC contamination (Chew et al. 2011; Huang et al. 2011). Although the various SST products available reflect the result of different cloud-clearing algorithms, evidence within the cited literature suggests strongly that passive IR radiometric algorithms exhibit little skill in detecting OTC.

Residual cirrus clouds present a significant concern for IR SST retrievals due to their high effective altitude, cold cloud tops, and relatively high occurrence, causing greater potential for significant radiance contamination and aliasing at IR wavelengths than atmospheric aerosols. To date, the potential for cirrus contamination and cold biasing of IR satellite-retrieved SSTs has been discussed only qualitatively (e.g., Merchant and Le Borgne 2004; Vázquez-Cuervo et al. 2004; Hosoda 2011; Merchant et al. 2012). SST bias from unscreened aerosols has been demonstrated (e.g., Merchant et al. 1999; Vázquez-Cuervo et al. 2004; Bogdanoff et al. 2015). Like OTC, aerosols act as strong longwave emission sources that contaminate sea surface emission signals and SST retrievals. However, significant aerosol plumes, like dense dust storms, occur less frequently and over limited domains compared with cirrus. Further, they are most prominent at significantly lower altitudes, which results in less thermal contrast with the sea surface and a relatively lower associated SST cold bias overall.

NASA's A-Train presents a unique opportunity for the pairing of IR radiometric and active-based remote sensing instruments, using *Aqua* and the *Cloud–Aerosol Lidar and Infrared Pathfinder Satellite Observations* (*CALIPSO*; Stephens et al. 2002; Winker et al. 2009, 2010) satellites, for investigating the cold biasing by OTC of IR SST retrievals (Huang et al. 2013). This paper describes a series of such experiments, using paired MODIS/Cloud Aerosol lidar with Orthogonal Polarization (CALIOP (Winker et al. 2010) measurements observations first to identify residual OTC contamination properties within the MODIS SST retrieval product and then to estimate corresponding SST cold biases for NLSST and triple-window IR algorithms developed for MODIS, VIIRS, and AVHRR.

Similar to Bogdanoff et al. (2015), a one-dimensional radiative transfer model is used to simulate SST retrieval algorithm performance by modeling OTC contamination for the different sensors, methodologies, and corresponding channels. MODIS/CALIOP cloud contamination properties are assumed consistent across VIIRS and AVHRR to motivate these modeling experiments. The goal of this work is a broad-scale assessment of the impact of OTC on operational IR radiometric satellite oceanographic sensors. We focus on tropical latitudes (30°S–30°N) in this investigation, given the greater occurrence frequencies for cirrus found there and thus presumably greater cold biasing of SST, relative to global conditions (Mace et al. 2009).

2. Datasets

a. *IR cloud-clearing and residual cloud contamination*

Quality testing and cloud clearing for the retrieval algorithms of each sensor vary slightly and stem from the tests created for the AVHRR Pathfinder algorithm described in Kilpatrick et al. (2001). For example, the MODIS cloud-clearing and quality control algorithm is based upon the use of brightness temperature difference, thresholds, and spatial homogeneity from IR measurements within the atmospheric window region. If a pixel passes the previous tests, then the retrieved SST is required to be within a specific range of the expected SST (from climatology or previous retrieval; Brown et al. 1999). The VIIRS cloud algorithm is identical to the MODIS algorithm, based upon the Miami Decision Tree (Minnett et al. 2013). The AVHRR, MODIS, and VIIRS retrieval algorithms reference both IR and visible channels for cloud clearing through threshold and spatial homogeneity tests (Lavanant et al. 2007).

Whereas collocation is possible only between CALIOP and MODIS, we are unable to independently characterize VIIRS and AVHRR cloud-clearing efficacies. Modeling of OTC bias in those datasets, described in sections 3 and 4, requires some knowledge of contaminating OTC properties, however. Thus, as introduced above, it is assumed that OTC contamination is consistent across the three sensors. Contamination properties relating cloud-top heights and relative frequencies from MODIS/CALIOP are thus extrapolated to VIIRS and AVHRR. However, product users presently face the question of whether to have available a daily satellite SST dataset with reasonable global coverage, at the expense of OTC contamination, or to face a highly limited dataset with many data points removed from fear of such bias.

b. *Infrared satellite SST products and retrieval models*

Daily 1-km 11- and 12-μm retrieved NLSST values from the Level 2 *Aqua* MODIS SST product (MOD28; available at https://oceandata.sci.gsfc.nasa.gov/MODIS-Aqua/L2) from January through December 2012 are used to collocate with CALIOP. To our knowledge, there is currently no MODIS triple-window retrieval. CALIOP is in orbit approximately 2 min behind *Aqua*-MODIS. Each MODIS SST retrieval is assigned a quality level (QL) between 0 and 4 (0 indicating no quality flags set or no known retrieval errors; 4 indicating a failed retrieval). QL is determined through a series of tests, specifically spatial homogeneity tests (i.e., pixel-by-pixel ''buddy checks''), climatology-deviation tests to remove unrealistic values, and baseline-deviation checks that look to filter values that represent a clear deviation from the weekly Optimum Interpolation Sea Surface Temperature (OISST; Reynolds and Smith 1994; Brown et al. 1999). The inclusion of these tests, beyond simple cloud clearing, suggests low confidence in the base visible and IR cloud detection. We are aware of no defined operational protocols for working with the MODIS NLSST product. In this study, we therefore assume that QL = 0 and QL = 1 are of sufficient fidelity so as to be referred to as quality-assured (QA) data. In contrast, QL > 1 is considered to represent retrievals with significant deviations from climatology or baseline values that are sufficiently indicative of some form of contamination (most likely cloud). A summary of the MODIS NLSST product, QL flags, and tests is available online (https://oceancolor.gsfc.nasa.gov/atbd/sst/). Results of the modeling experiments described below are shown for each of QL=0, QL=1 and QA for completeness.

Pathfinder-style MODIS IR NLSST retrievals are conducted using measured radiances at the 11.03- and 12.02-μm bands, chosen as they exhibit significant differences in water vapor absorption and proximity to the average planetary blackbody emission temperature (Brown et al. 1999). Retrievals are performed through the following system of equations (Brown et al. 1999): for $\Delta T_B \leq 0.5$:

$$\mathrm{SST} = a_{00} + (a_{01}T_{B_{11}}) + (a_{02}\Delta T_B\overline{\mathrm{SST}}) + \left[a_{03}\Delta T_B\left(\frac{1.0}{\mu} - 1\right)\right]; \tag{1a}$$

for $\Delta T_B \geq 0.9$:

$$\mathrm{SST} = a_{10} + (a_{11}T_{B_{11}}) + (a_{12}\Delta T_B\overline{\mathrm{SST}}) + \left[a_{13}\Delta T_B\left(\frac{1.0}{\mu} - 1\right)\right]; \tag{1b}$$

for $0.5 \leq \Delta T_B \leq 0.9$:

$$\mathrm{SST} = \mathrm{SST}(\Delta T_B \leq 0.5) + \frac{(\Delta T_B - 0.5)}{(0.9 - 0.5)}[\mathrm{SST}(\Delta T_B \geq 0.9) - \mathrm{SST}(\Delta T_B \leq 0.5)]. \tag{1c}$$

Here, ΔT_B is the difference between the brightness temperature at the 11- and 12-μm bands; $T_{B_{11}}$ is the brightness temperature (°C) at the 11.03-μm band; μ is the cosine of the sensor zenith angle; $\overline{\mathrm{SST}}$ is a baseline SST value created by bilinear interpolation of the OISST product or a near-IR retrieved SST value (from the previous night); $\mathrm{SST}(\Delta T_B \leq 0.5)$ and $\mathrm{SST}(\Delta T_B \geq 0.9)$ are the SST values calculated using Eqs. (1a) and (1b), respectively; and the a coefficients are continuously tuned and optimized through verification with in situ buoy observations.

Uncertainties arise in the derivation of operational coefficients due to ambiguities in relating buoy observations with satellite radiances and the possible presence of OTC. For simulations of this retrieval described in section 3, the a coefficients from the most recent July available (2006) are used: $a_0 = 1.2310$; $a_1 = 0.9470$; $a_2 = 0.1680$; $a_3 = 1.8170$; $a_{10} = 2.5450$; $a_{11} = 0.9050$; $a_{12} = 0.1250$; $a_{13} = 1.6660$. The July coefficients are used to be consistent with the coefficients used for the VIIRS retrievals.

The *MetOp-A* AVHRR NLSST retrieval is performed using radiances at the 10.8- and 11.9-μm bands, from channels 4 and 5, using the following equation from the Naval Oceanographic Office (NAVO) NLSST algorithm (Walton et al. 1998):

$$\mathrm{SST} = a_0 + (a_1T_{B_{11}}) + (a_2\Delta T_B\overline{\mathrm{SST}}) + \left[a_3\Delta T_B\left(\frac{1.0}{\mu} - 1\right)\right], \tag{2}$$

where $T_{B_{11}}$ is the brightness temperature (K) from the 10.8-μm band, ΔT_B is the difference in brightness temperatures between the 10.8- and 11.9-μm bands, and the coefficients a_1, a_2, and a_3 are tuning constants, again based on optimization between retrievals and observations from global drifting buoys. We apply the set of operational coefficients provided by NAVO and used by Bogdanoff et al. (2015) to model the retrieval ($a_0 = -263.3489$; $a_1 = 0.9690$; $a_2 = 0.0772$; $a_3 = 1.0318$).

The *Suomi-NPP* VIIRS NLSST retrieval algorithm applies radiances at the 10.80- and 12.05-μm bands from channels 15 and 16 to retrieve SST (Brisson et al. 2002; Merchant et al. 2008; Petrenko et al. 2014), using the equation

$$\mathrm{SST} = a_0 + (a_1T_{B_{11}}) + \left(a_2T_{B_{11}}\frac{1.0}{\mu}\right) + (a_3\Delta T_B) + (a_4\Delta T_B\overline{\mathrm{SST}}) + \left(a_5\Delta T_B\frac{1.0}{\mu}\right) + \left(a_6\frac{1.0}{\mu}\right), \tag{3}$$

where $T_{B_{11}}$ is the brightness temperature (K) from channels 15; ΔT_B is the difference in brightness temperatures in the 10.80- and the 12.05-μm bands; $\overline{\mathrm{SST}}$ is Level 4 SST (°C), provided by the Canadian Meteorological Centre (or another Level 4 SST product if unavailable); and the coefficients a_0–a_6 are again the optimized tuning constants. The set of coefficients used to model the retrieval here come from the Advanced Clear-Sky Processor for Oceans (ACSPO) SST algorithm as of July 2015 (B. Petrenko 2015, personal communication; $a_0 = 5.623\,045$; $a_1 = 0.985\,192$; $a_2 = 0.019\,775$; $a_3 = 0.456\,758$; $a_4 = 0.067\,732$; $a_5 = 0.705\,117$; $a_6 = -4.714\,369$).

Algorithms using triple-window retrieval techniques are also available for AVHRR and VIIRS. The *MetOp-A* AVHRR triple window SST is retrieved using

$$\begin{aligned}\mathrm{SST} = a_0 &+ \left\{a_1 + \left[a_2\left(\frac{1.0}{\mu} - 1\right)\right]\right\}T_{B_{3.7}} \\ &+ \left\{a_3 + \left[a_4\left(\frac{1.0}{\mu} - 1\right)\right]\right\}\Delta T_B \\ &+ \left[a_5\left(\frac{1.0}{\mu} - 1\right)\right], \qquad (4)\end{aligned}$$

where $T_{B_{3.7}}$ is the brightness temperature (°C) from the 3.7-μm band, ΔT_B is the difference in brightness temperatures between the 10.8- and 11.9-μm bands, and the coefficients a_1–a_5 are again tuning constants. For modeling the retrieval below, we apply a set of coefficients described by Météo-France ($a_0 = 1.153\,51$; $a_1 = 1.018\,67$; $a_2 = 0.021\,09$; $a_3 = 0.688\,58$; $a_4 = 0.330\,56$; $a_5 = 1.273\,03$; Le Borgne et al. 2007).

The operational NAVO *Suomi-NPP* VIIRS triple window algorithm uses the same equation as the *MetOP-A* AVHRR triple window SST retrieval, where ΔT_B is the difference in brightness temperatures between 10.80- and 12.05-μm bands. Here, we model this equation by applying a set of operational coefficients from the ACSPO SST algorithm as of July 2015 (B. Petrenko 2015, personal communication; $a_0 = 0.236\,653$; $a_1 = 1.003\,204$; $a_2 = 0.032\,301$; $a_3 = 0.992\,169$; $a_4 = 0.241\,534$; $a_5 = -8.055\,822$).

c. *CALIOP cirrus cloud products*

CALIOP cirrus cloud observations considered here come from the version 3.02 (V3.02) Level 2 *CALIPSO* 5-km cloud layer product (https://eosweb.larc.nasa.gov/). This product includes cloud-top and cloud-base heights, corresponding temperatures, and COD. Cloud temperatures come from the Goddard Modeling and Assimilation Office (GMAO)'s Goddard Earth Observing System Model, version 5, data embedded within the file. This product is chosen for its integration of resolved cloud layers at multiple spatial resolutions (5, 20, and 80 km; Vaughan et al. 2009), which more readily include OTC. Clouds resolved with CALIOP algorithms at higher resolution (0.33 and 1.00 km) are not included in this product, as they likely represent spatially inhomogeneous liquid water clouds and not cirrus. Given that cloud contamination statistics in the collocated *Aqua*-MODIS/CALIOP subset are shown below, however, this caveat with respect to relative frequencies in liquid-phase cloud contamination exists, particularly for the lowest/warmest cloud cases reflective of marine stratocumulus decks.

Cirrus clouds are specifically distinguished in the CALIOP dataset by applying a maximum cloud-top temperature of −37°C. The basis for applying this thermal threshold is motivated by Campbell et al. (2015). Though conservative, significant ambiguity arises from interpreting autonomous lidar signals and from distinguishing "warm cirrus" (typically, sheared fallstreaks decoupled from their parent cloud, which give the appearance of a cirrus cloud with an apparent top height temperature warmer than −37°C) from glaciated liquid water clouds that, though ice, are not cirrus in the phenomenological sense. These latter clouds feature ice microphysical characteristics that are sufficiently different from traditional cirrus, such that their optical and radiative characteristics warrant a distinct phenomenological classification in their own right, particularly given the constraints of the radiative transfer modeling experiments conducted and described here (e.g., Sun and Shine 1994). This distinction is fundamental to optimizing the radiative transfer model simulations described below, since they are based upon parameterized cirrus cloud ice microphysical properties specifically, as opposed to those of glaciated cloud elements.

COD is used below as the dependent variable for estimating SST retrieval cold biases. COD uncertainties in the V3.02 product have been recently characterized by Garnier et al. (2015). Specifically, CALIOP COD algorithms perform either constrained retrievals, where COD is solved directly by comparing molecular atmospheric backscatter returns above and below the cloud, or unconstrained ones, where molecular returns below the cloud cannot be estimated and an a priori relationship between cloud extinction and backscatter coefficients is applied based on cloud centroid temperature to solve COD (Vaughan et al. 2009; Young and Vaughan 2009). Whereas we are dealing almost exclusively with relatively low COD cases with OTC, our sample compositions tends strongly toward constrained retrievals for which we anticipate relatively low relative error.

3. Methodology

a. *MODIS–CALIOP collocation and cloud contamination*

MODIS SSTs are reported at 1-km^2 spatial resolution. Collocation between *Aqua*-MODIS and the 5-km CALIOP product is performed by identifying those QA MODIS SST 1-km^2 pixel centers within 1 km of the lidar ground track. The frequency of contamination is reported by cloud type (all cirrus, OTC, and other) and QA level. Residual cloud-top altitudes, temperatures, and COD are also examined. Contamination statistics are described in section 4.

b. Modeled SST bias due to optically thin cirrus

OTC cold bias estimates for each of the satellite retrievals are estimated through radiative transfer simulations using the Santa Barbara DISORT Atmospheric Radiative Transfer (SBDART) model (Ricchiazzi et al. 1998). Following Bogdanoff et al. (2015), top-of-atmosphere radiance values for sensor nadir are calculated using SBDART as equipped with a standard tropical atmosphere and a surface and skin temperature of 26.85°C (300 K), which is used as the background SST. SST cold bias is defined as the difference between an SBDART-simulated OTC-contaminated SST retrieval and an SBDART-simulated clear-sky SST retrieval. In other words, the SBDART surface skin temperature of 26.85°C is not used. Instead, an SBDART-simulated clear-sky SST retrieval is used. This clear-sky value is then subtracted from the SBDART-simulated OTC-contaminated SST retrievals. In this way, the bias is only a function of the introduction of the OTC but also not dependent on the retrieval equation's ability to reproduce the SBDART profile skin temperature of 26.85°C.

The MODIS-, VIIRS-, and AVHRR-simulated brightness temperatures are calculated by integrating the SBDART-estimated radiance with each sensor's spectral response function. The MODIS 11.30-μm band radiance is calculated from the SBDART 10.50–11.50-μm radiances in 100-nm increments. The MODIS 12.02-μm band radiance is calculated from the SBDART 11.64–12.44-μm radiances, also in 100-nm increments. The AVHRR 10.80- and 11.90-μm band radiances are calculated from the SBDART 10.10–11.60- and 11.20–12.60-μm radiances in 100-nm increments, respectively. Likewise, the VIIRS 10.80- and 12.05-μm radiances are calculated from the SBDART 9.90–11.70- and 11.06–12.76-μm radiances in 100-nm increments. The AVHRR and VIIRS 3.7-μm band radiances are calculated from SBDART-simulated nighttime 3.40–4.00- and 3.50–3.90-μm radiances in 20-nm increments, respectively. All increments represent slightly higher than what is resolvable by SBDART and thus some interpolation is performed.

A two-dimensional SST cold bias matrix is determined for MODIS, VIIRS, and AVHRR NLSST and VIIRS and AVHRR triple-window retrievals after simulating a 1.5-km-thick OTC layer present at varying top height altitudes [10.00–18.00 km in 0.25-km segments, all heights above mean sea level (MSL)] and COD (0.00–0.30, in 0.01 segments from 0.01–0.06 and 0.02 segments above 0.06). By default, SBDART vertical grid spacing is set to 1 km from the surface to 100 km. To resolve the 0.25-km segments, this grid spacing has been adjusted to vary from 0.25 km near surface to 30 km at 100 km. While the segments near 18 km are slightly larger than 0.25 km, the difference is on the order of 10 m. In this case, the cloud top is placed slightly above 18 km.

Mean OTC SST bias values are estimated by integrating the product of the frequency of OTC-only occurrence for each altitude/COD bin and the corresponding SST cold bias modeled with SBDART. Relative bias, defined as the mean bias of all OTC-only contaminated retrievals, is then calculated using only the relative frequency of occurrence. Finally, the absolute bias is the mean bias of all pixels, assuming only OTC contamination (i.e., relative bias normalized by the frequency of OTC occurrence) given by the absolute frequency of occurrence. As a subsequent sensitivity test, the proportionality between the difference between the true SST and brightness temperatures between 11- and 12-μm channels is examined for each sensor, given again that the NLSST technique is based upon the assumption that this relationship is relatively constant given constant integrated column water vapor. For bias estimation, the water vapor profile is unadjusted, except within the cloud. However, when this proportionality is examined, the water vapor profile is adjusted proportionally outside of the cloud, such that the total column water vapor is held constant.

The core SBDART module simulates cirrus clouds as spherical ice grains (Ricchiazzi et al. 1998). Yang et al. (2005), however, report that differing ice particle structures result in significant variance in absorption efficiency at the wavelengths used in the SST retrievals. Thus, we modified the SBDART ice microphysical scheme to be consistent with that of the ice particle structures defined in Yang et al. (2005). For particles with effective radius smaller than 35 μm, the augmented ice microphysical scheme assumes 50% bullet rosettes, 25% hollow columns, and 25% plates. For particles with an effective radius larger than 35 μm, the scheme assumes 30% aggregates, 30% bullet rosettes, 20% hollow columns, and 20% plates (Yang et al. 2005). Within cloud, SBDART features a method to adjust the water vapor such that the atmosphere is saturated with respect to liquid water. This method has been updated to saturate the layer with respect to ice if the temperature is below −37°C, and with respect to liquid water above this temperature using the Goff–Gratch equations and assuming water vapor to be an ideal gas.

The cloud structure is designed within the simulations such that radiances from both a cirrus cloud with a linearly increasing extinction coefficient from cloud base to top (i.e., a fallstreak) and a cloud with a constant extinction coefficient (i.e., "block" cloud) are solved independently. The block cloud and fallstreak structures were referred to as "infinite gradient" and "shelf gradient," respectively, in Bogdanoff et al. (2015). Sensitivity to cloud structure is found to be negligible, however, and only results from the fallstreak simulations are presented.

Sensitivity to ice crystal effective radius in SBDART is constrained using Eq. (9e) in Heymsfield et al. (2014). This provides a relationship between SBDART standard atmospheric temperature, altitude, and effective radius. Ice crystal effective radius is approximately 95 μm at an altitude of 10 km, dropping to near 10 μm × 16 km. Note that there is no normalizing of the actual MODIS/CALIOP-contaminated OTC observations as a function of height/temperature to the temperature profile of the standard atmosphere used to derive the net-integrated bias values. They are instead assumed independent. This will induce some representativeness error in the solutions, since the contaminated observations will not directly coincide with the temperatures and heights of the standard atmosphere.

Sensitivity of the SST error matrices to column water vapor concentrations is tested by adjusting the water vapor mixing ratio profile in the SBDART standard atmosphere during the simulations. Two tests are performed, aside from the direct solutions using the standard atmospheric water vapor profile. The first is conducted with the water vapor mixing ratio set to zero everywhere except within the cloud. The other test saturates the entire column with respect to liquid water at temperatures above -37°C and with respect to ice below that temperature. The purpose of this exercise is to provide ample context for considering the integrated bulk SST biases calculated from the error matrices, given that the impact of water vapor absorption and column-integrated instrument sensitivities within the SST retrievals themselves can be considerable (e.g., Brown et al. 1999).

c. *Observational representativeness*

To characterize the representativeness of the SBDART simulations and corresponding cold bias estimates, an analysis of contaminated MODIS data points is provided for a look at how bias relates in practice. It is believed that this is the most practical means to estimate bias. Advanced Microwave Scanning Radiometer (AMSR) microwave SSTs, for instance, are not biased by OTC presence, given the much longer wavelength than in the IR. However, AMSR data are not available for the 2012 study period. Furthermore, AMSR SSTs are retrieved at approximately 25-km^2 resolution, making them difficult to collocate with confidence to higher-resolution data from the IR radiometers. A single AMSR-retrieved SST pixel can correspond with as many as 625 MODIS pixels, for example. Buoy collocation with MODIS also could be attempted. However, the relative bias estimates introduced below are in fact approximately equal to that found between buoy subsurface temperature measurements and remotely sensed skin temperature retrievals (Brown et al. 1999).

Instead, linear regression is performed between *Aqua*-MODIS SST retrievals and CALIOP COD for OTC-contaminated retrievals over the Southeast Asian Maritime Continent (135°E, 30°N–75°E, 15°S) for August–October 2012. A limited spatial and temporal domain is chosen to mitigate any large spatial and seasonal variability, as sample spread limits the effectiveness of the target regressions. This result is then qualitatively compared with OTC SST bias estimates derived from the SBDART simulations to gauge how representative the bias estimates are in practice.

4. Analysis

a. *Collocation statistics*

Numbers of collocated QA *Aqua*-MODIS/CALIOP data points in 5° × 5° bins between 30°S and 30°N are shown in Fig. 1. Although large spatial variation in pixel counts is evident, bins with relatively low data counts (such as the Southeast Asian Maritime Continent) still contain nearly 10 000 collocated points. The spatial variability in valid collocations varies in both the availability of QA data, which can be limited due to cloud or other forms of radiance contamination of the MODIS retrieval (manifested in the QL value, and discussed in further detail below), and OTC occurrence. Figure 2a depicts corresponding total all-cloud contamination frequencies for the collocated data points. Of particular interest is the Maritime Continent, where cloud is present in upward of 80% of all collocated data pairs. A comparison of cirrus contamination with all-cloud contamination (Fig. 2b) shows that the majority (>90%) of all residual cloud is cirrus, though this is likely influenced to some degree by the composition of the Level 2 CALIOP dataset used (discussed in section 2c); 99.4% of the cirrus sample is OTC (25.7% absolute frequency). These distributions and percentages of cirrus contamination closely match expectation (see Fig. 1 in Sassen et al. 2008).

To determine the relative contamination characteristics for each oceanic basin, every 5° × 5° bin is associated with its parent ocean (Fig. 3). Bins that overlap both the Atlantic and Pacific basins, such as bins over Central

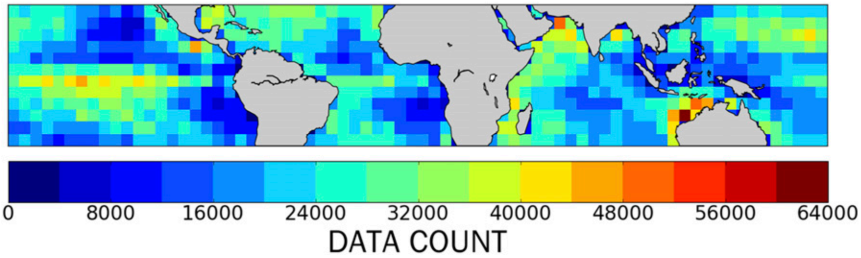

FIG. 1. Number of collocated Level 2 *Aqua*-MODIS SST and Level 2 CALIOP cloud-profiling pixels for MODIS data QL = 0 and QL = 1, in 5° × 5° bins between 30°S and 30°N.

America, are not included in the basin investigation. This is deemed unnecessary for the boundary between the Indian and Pacific basins because that boundary is less defined than the distinct geographical barrier presented by Central America for the Pacific–Atlantic boundary. Following Fig. 4, then, is the corresponding difference between the raw QA MODIS SST product and that after cloud clearing with CALIOP, whereby the corresponding cold bias effect due to overwhelming OTC presence is realized.

Histograms of cloud-top heights and temperatures for residual clouds identified with CALIOP from the collocated *Aqua*-MODIS data pairs in each basin are presented in Figs. 5a and 5b, respectively. These plots exhibit a bimodal distribution between high-altitude cold clouds and near-surface warm clouds, echoing Toth et al. (2013). The Atlantic basin corresponds with, on average, warmer and lower cloud tops, with more low-level cloud contamination than the other basins. This is likely due to cooler SSTs in the Atlantic basin, resulting in lower tropopause heights and lesser influence on ice particle nucleation from the tropical tropopause transition layer (TTL; Fueglistaler et al. 2009). The Pacific and Indian Oceans exhibit very similar residual cloud properties, which is likely a reflection of both basins sharing the very warm waters in and around the Maritime Continent.

All basins correspond with a relatively strong residual cirrus signal. Retrieval contamination statistics are outlined in Table 1, distinguished by MODIS retrieval QL and oceanic basin. Globally, the majority of collocations (>76%) are QL = 0. These "best quality" retrievals still experienced OTC cloud contamination at a rates of nearly 23%, while the lower QL = 1 data experienced OTC contamination at approximately 36%. This results in an overall QA dataset OTC contamination rate of ~26% throughout the tropics.

OTC COD occurrence histograms for contaminated data pairs in each basin are shown in Fig. 6. Similar to OTC distributions derived globally from CALIOP, shown in Campbell et al. (2015), residual COD occurrence across all basins decreases exponentially with increasing COD, with counts in the "subvisual" range (COD < 0.03; Sassen and Cho 1992) occurring two

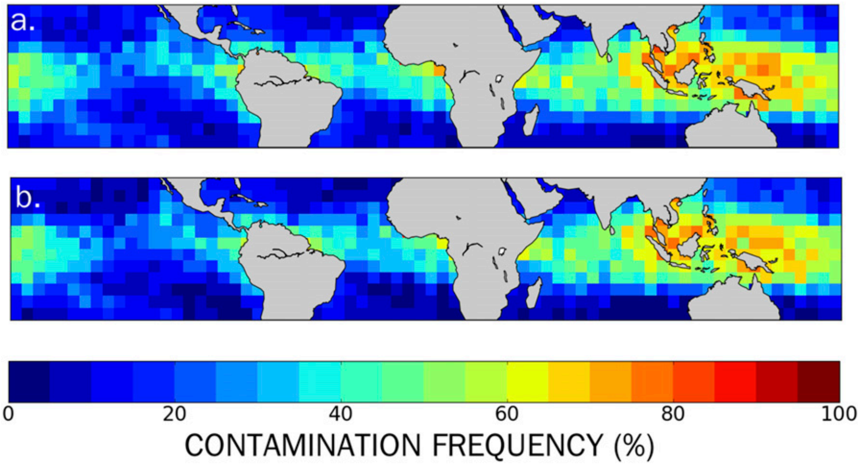

FIG. 2. Relative frequencies of collocated *Aqua*-MODIS SST retrieval contamination, as identified by CALIOP for (a) all cloud and (b) all cirrus (defined as all clouds with a top height temperature ≤ −37°C).

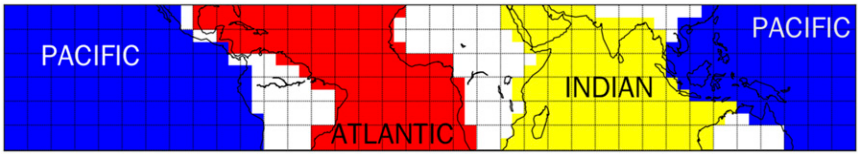

FIG. 3. Spatial extent of oceanic basins used in this study with corresponding 5° × 5° bins depicted from 30°S and 30°N.

orders of magnitude more often than those approaching the upper-OTC COD threshold near 0.30. All cirrus and OTC COD statistics globally and for each basin are presented in Table 1. Mean contaminating OTC COD globally is near 0.04. Despite lower/warmer clouds, the Atlantic basin coincides with the optically thinnest clouds. Further, and as expected, QL = 1 clouds are optically thicker than QL = 0, consistent with the greater expectation of cloud contamination that would likelier reflect the presence of denser clouds.

b. NLSST bias estimates

Respective OTC-only NLSST cold bias matrices are shown for *Aqua*-MODIS (Fig. 7a), AVHRR (Fig. 7b), and VIIRS (Fig. 7c). Overlaid on these data are relative occurrence percentages of cloud contamination from *Aqua*-MODIS/CALIOP. Net OTC cold bias is estimated by integrating the product of relative/absolute frequency and corresponding bias at each bin as functions of cloud-top height and COD. Again, we emphasize for AVHRR and VIIRS that this step assumes that OTC cloud-clearing algorithm infidelities are reasonably consistent across each sensor.

The SBDART simulations, and thus all corresponding bias estimates, are conducted only for the nadir view of either sensor. Assuming that OTC contamination occurrence rates are relatively consistent at all viewing angles though as a function of COD (which, given the complexities of passive cloud screening algorithms, such as ‘‘buddy check’’ pixel comparisons, may very well not be a good assumption at all), an expanded study could take into account varying passive sensor responses to the viewing angles. Given that the relative COD will effectively increase with greater viewing angle however, from increased optical pathlength through the clouds relative to the sensor, such a study would become far more complex than the basic conceptualization conducted here.

Evident in the cold bias simulations is the sensitivity to both altitude (i.e., cloud effective radius and thermal brightness) and COD (i.e., ice water path). Each sensor retrieval algorithm exhibits generally negligible bias at subvisual COD (Sassen and Cho 1992). All sensors exhibit maximum bias at CODs approaching 0.3 and cloud-top altitudes below 15 km, corresponding to effective cloud particle radii greater than 25 μm. This maximum indicates a bias > 6°C for MODIS, AVHRR, and VIIRS retrievals. Note that some undersampling in the absolute/relative OTC cold bias estimates derived from these data arises and is apparent here. SBDART simulations are conducted only between 10.0 and 18.0 km. The lower threshold coincides approximately with −37°C on the tropical standard atmospheric profile used in SBDART, which is the thermal threshold used to distinguish cirrus clouds in the CALIOP sample (described further above). The upper threshold is actually 1 km above the cold-point tropopause height in the standard atmospheric profile used as indicated by the increase in bias above 17.0 km.

It is relatively common to see cirrus clouds in the tropics, particularly TTL cirrus, at and above 18.0 km (e.g., Campbell et al. 2015, among many others). This upper threshold is adjusted slightly from the standard atmosphere cold-point tropopause accordingly. Reality,

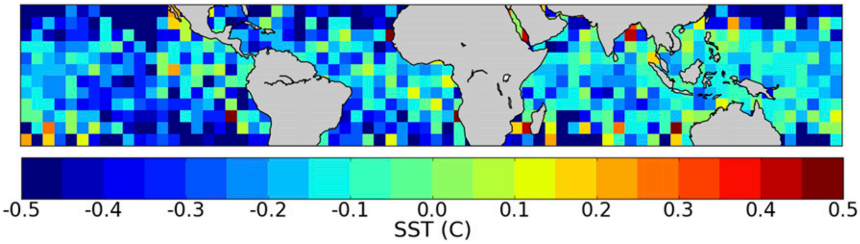

FIG. 4. For collocated *Aqua*-MODIS SST and CALIOP cloud profile data pairs, with the absolute difference between the raw QA product and that after cloud screening.

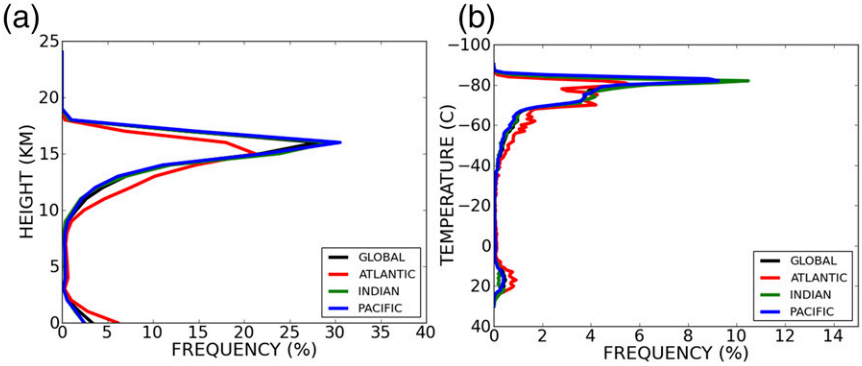

FIG. 5. Relative frequencies of all residual cloud found in contaminated Level 2 *Aqua*-MODIS SST and CALIOP cloud profile data pairs as a function of (a) cloud-top height and (b) cloud-top temperature, plotted globally and for the Atlantic, Indian, and Pacific Ocean basins (see insets).

however, causes some cirrus, and specifically OTC, to be observed by CALIOP outside of this range within the tropics, which are included in the OTC-contaminated *Aqua*-MODIS/CALIOP sample; 1.07% of the tropical OTC sample is not accounted for when integrating the cold bias matrices and deriving final estimates, suggesting the results are slightly low. However, the increase in atmospheric temperature results in larger particles and more bias above this cold point, suggesting the results may be high. Combined with the assumptions of cloud contamination consistency across each sensor/algorithm and the use of a static tropical standard atmosphere/static surface SST in deriving the initial cold bias matrices, we reiterate that these solutions are strictly estimates.

Cold bias estimates are reported in Tables 2 and 3 for each sensor, based upon the *Aqua*-MODIS QL and the oceanic basin. Ranges of bias associated with water vapor sensitivity are also reported according to the supplemental experiments described in section 3b. The mean absolute global QA OTC-only SST cold bias estimated across the three platforms from these simulations without varying the relative humidity profile from that of the standard atmosphere is between 0.09° and 0.14°C. This range reflects the absolute aggregate cold bias estimated for each sensor in bulk-average tropical SST, given OTC-only contamination occurrence rates on the order of 25%. The corresponding relative bias ranges from 0.33° to 0.55°C, reflecting the mean cold bias specifically for OTC-contaminated single observations.

TABLE 1. Collocated data counts—all-cloud, all-cirrus, and OTC contamination statistics—calculated from *Aqua*-MODIS/CALIOP collocation globally and for the Atlantic, Indian, and Pacific Ocean basins. Quality control refers to the MODIS QL = 0 and QL = 1 Level 2 datasets used for collocation with CALIOP.

Quality		Global	Atlantic	Indian	Pacific
QL = 0	Data count	11 638 397	2 185 709	2 746 064	5 750 944
	All-cloud contamination (%)	24.75	20.45	26.81	27.64
	Cirrus contamination (%)	22.63	17.66	25.06	25.64
	OTC fraction (%)	99.70	99.70	99.75	99.66
	Mean OTC COD	0.034	0.033	0.034	0.034
QL = 1	Data count	3 569 473	701 492	774 006	1 870 591
	All-cloud contamination (%)	39.78	35.62	43.79	41.48
	Cirrus contamination (%)	36.40	31.47	40.74	38.41
	OTC fraction (%)	98.86	99.15	98.83	98.75
	Mean OTC COD	0.054	0.047	0.056	0.055
TOTAL QC	Data count	15 207 870	2 887 201	3 520 070	7 621 535
	All cloud contamination (%)	28.28	24.14	30.54	31.04
	Cirrus contamination (%)	25.86	21.01	28.50	28.77
	OTC fraction (%)	99.42	99.50	99.46	99.37
	Mean OTC COD	0.041	0.038	0.041	0.041

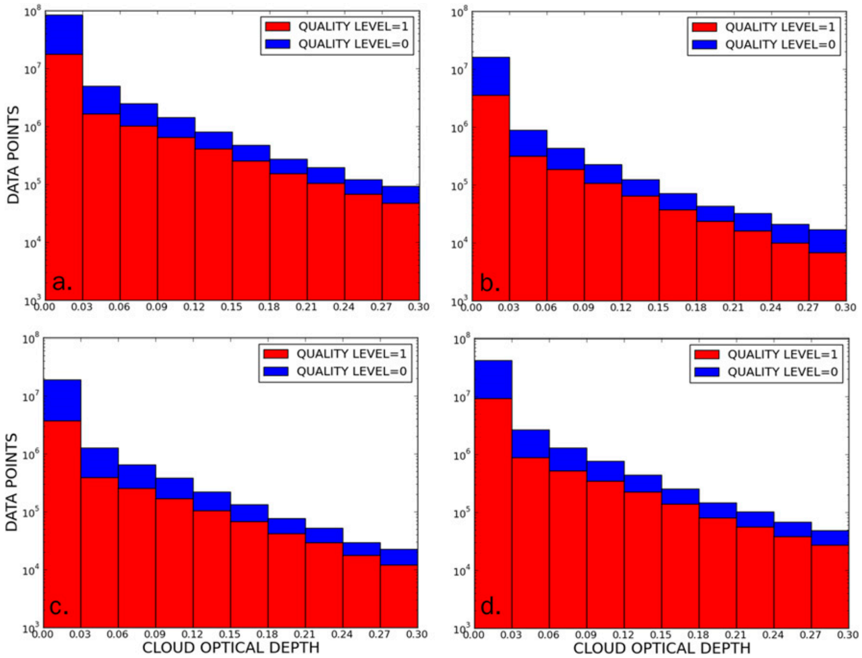

FIG. 6. Histograms of residual optically thin cirrus (OTC) cloud optical depths (COD) for *Aqua*-MODIS SST QL = 0 and QL = 1 (see insets) for (a) global, and (b) Atlantic, (c) Indian, and (d) Pacific Ocean basins.

MODIS represents the lowest bias followed by VIIRS and AVHRR, the latter having approximately 65% higher bias. Relative cold biases are higher, reflecting the impact of a single event as opposed to one normalized by its absolute occurrence rates.

Water vapor sensitivity is relatively stable across the three sensors, with AVHRR exhibiting less variance than MODIS or VIIRS. Interestingly, for the highest-quality data (QL = 0), the standard atmosphere represents lower bias for MODIS than that of either the dry or saturated case. This may be the result of the coefficients in the Pathfinder-style equation being tuned for more realistic column water vapor values. Values derived for the perturbed water vapor mixing ratio profiles relative to the standard atmosphere encompass the two sets of simulations as lower and higher bounds, respectively.

Figure 8 features MODIS-only cold bias composites and relative OTC contamination rates for the Atlantic Ocean (Fig. 8a), Indian Ocean (Fig. 8b), and Pacific Ocean (Fig. 8c) basins (see Fig. 3). Again, the Indian and Pacific Ocean basins exhibit relatively similar distributions, with the Atlantic Ocean profile being much more broadly distributed in terms of relative percentage frequency with height.

Absolute/relative cold bias estimates for the Indian and Pacific Ocean basins, from Tables 2 and 3, are relatively constant across the three sensors. The absolute cold bias is lower, in contrast, over the Atlantic Ocean due to lower OTC occurrence frequencies. Interestingly, however, relative cold biases are higher in the Atlantic basin. This is due to OTC generally occurring at lower heights, which corresponds with lower cloud-top temperatures and larger effective cloud radii. This result has important ramifications, though. This implies that, despite a lesser absolute occurrence rate anticipated outside of the tropical latitudes, relative OTC SST contamination will likely persist at significant cold bias values outside of the tropics overall. It is plausible that absolute bias could in fact be equal to or exceed that of the tropics. Despite conceptualizing this OTC SST contamination problem within a single zonal domain, the effect likely persists globally in equal, if not greater, significance.

Figure 9 depicts the ratio of the difference between the retrieved clear-sky SST and the OTC-contaminated brightness temperatures modeled for each sensor in SBDART from the corresponding near-11- and near-12-μm bands. As NLSST algorithms are based upon the assumption that these differences are proportional and constant for a given water vapor loading, the significant variance depicted in each sensor illustrates how susceptible the retrievals are to the presence of OTC overall [a similar response was illustrated by Merchant et al. (1999) for stratospheric volcanic aerosols]. We reiterate, for these simulations, that the profile water vapor is proportionally decreased outside of the cloud,

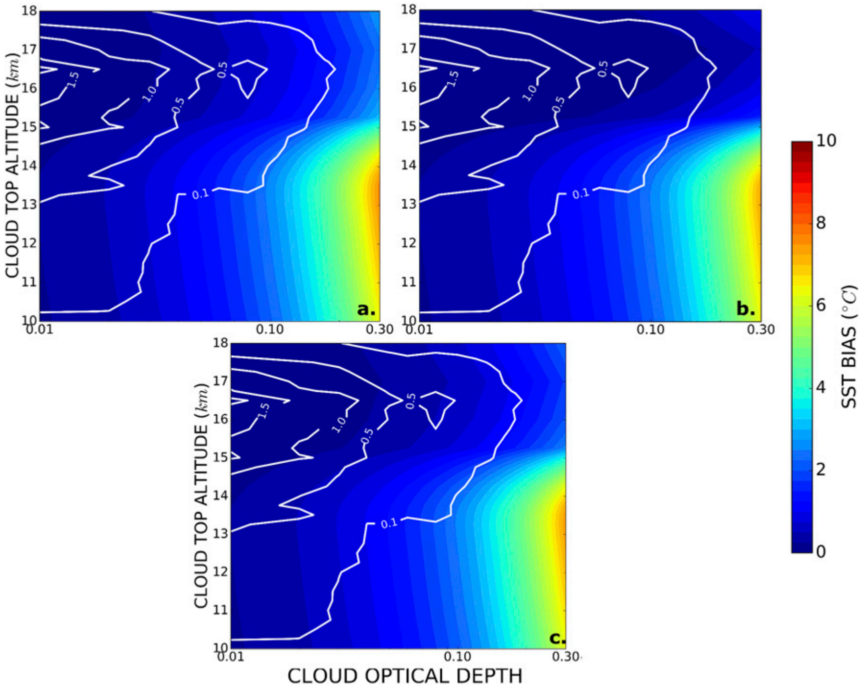

FIG. 7. SBDART radiative transfer model simulations of potential SST retrieval cold bias for an unscreened OTC as a function of cloud-top height and optical depth for (a) AVHRR, (b) MODIS, and (c) VIIRS. Overlaid on each composite are relative *Aqua*-MODIS/CALIOP collocated cirrus contamination occurrence frequencies (%).

such that total column water vapor is held constant throughout all the simulations. All sensors exhibit variance, suggesting this NLSST developmental assumption fails in the presence of OTC. MODIS and AVHRR exhibit similar variance, ranging from approximately 0.7 to 0.9. VIIRS ranges from approximately 0.8 to 0.95. A low difference between proportionality at high COD when compared to low COD corresponds with lower theoretical cloud bias. This is because the thicker clouds are acting similar to thin clouds from an algorithm standpoint. Interestingly, the proportionality in VIIRS is of a different structure than MODIS or AVHRR above 15 km. Furthermore, the VIIRS proportionality is offset closer to 1 than the other sensors. This may be due to differences in sensor design. For example, the VIIRS 12-μm band is shifted toward shorter wavelengths when compared to AVHRR and MODIS.

c. *Triple-window bias estimates*

Triple-window OTC cold bias matrices and absolute and relative bias estimates for AVHRR and VIIRS are presented in Fig. 10 and Table 4, respectively. Again, to our knowledge no MODIS triple-window product is publicly available. The bias structure is similar to the NLSST for both sensors, though the VIIRS simulations now exhibit the secondary maximum in bias above 15 km. The triple-window algorithms prove less susceptible to cirrus contamination than NLSST in terms of bias magnitude, however. Global AVHRR absolute and relative biases are estimated at 0.02° and 0.08°C, respectively, which unlike NLSST are lower than for VIIRS (0.04° and 0.14°C, respectively). Bias estimates drop $>$ 90% for VIIRS and AVHRR overall. Thus, triple-window techniques exhibit much greater resilience to OTC, in spite of their traditionally being limited to nighttime use only. With relative bias ranging from 0.10° to 0.15°C overall across all basins, the product is significantly more stable for operational use than the NLSST. Because of the relatively low bias estimates, a water vapor sensitivity analysis is not performed here.

d. *Verification*

To gauge the representativeness of the SBDART-modeled OTC cold bias estimates, a comparison with available observations is performed. Figure 11 depicts a scatterplot of OTC-contaminated SST versus COD over the Southeast Asian Maritime Continent (75°E, 15°S –135°E, 30°N) for August–October 2012. The premise is that the slope of a linear regression fit to these data should approximately equal that relationship between the cold bias and OTC COD estimated from Fig. 7. The slope calculated from these data is −6°C per COD or

TABLE 2. Mean absolute (bulk mean) OTC cold biases in MODIS, AVHRR, and VIIRS NLSST retrievals from SBDART simulations and assuming *Aqua*-MODIS/CALIOP collocated contamination frequencies, for OTC block cloud extinction and fallstreak extinction coefficient gradients applied in the simulations (see text), segregated as a function of QL, global, and Atlantic, Indian, and Pacific Ocean basins. Absolute OTC cold biases for the atmospheric profile with no water vapor and for the saturated column are given in parentheses.

Sensor	QL	Global	Atlantic	Indian	Pacific
MODIS	0	0.06°C (0.06°–0.11°C)	0.06°C (0.06°–0.09°C)	0.06°C (0.07°–0.12°C)	0.06°C (0.07°–0.11°C)
	1	0.17°C (0.16°–0.27°C)	0.16°C (0.15°–0.24°C)	0.19°C (0.17°–0.31°C)	0.16°C (0.15°–0.27°C)
	QA	0.09°C (0.09°–0.14°C)	0.08°C (0.08°–0.13°C)	0.09°C (0.09°–0.16°C)	0.09°C (0.09°–0.15°C)
AVHRR	0	0.10°C (0.10°–0.13°C)	0.09°C (0.08°–0.11°C)	0.12°C (0.11°–0.14°C)	0.11°C (0.11°–0.14°C)
	1	0.27°C (0.25°–0.32°C)	0.23°C (0.22°–0.27°C)	0.30°C (0.28°–0.37°C)	0.27°C (0.25°–0.33°C)
	QA	0.14°C (0.13°–0.17°C)	0.13°C (0.12°–0.15°C)	0.16°C (0.15°–0.19°C)	0.15°C (0.14°–0.19°C)
VIIRS	0	0.09°C (0.08°–0.12°C)	0.08°C (0.07°–0.10°C)	0.10°C (0.09°–0.13°C)	0.10°C (0.09°–0.13°C)
	1	0.23°C (0.21–0.29°C)	0.21°C (0.19°–0.26°C)	0.26°C (0.24°–0.34°C)	0.23°C (0.21°–0.30°C)
	QA	0.12°C (0.11–0.16°C)	0.11°C (0.10°–0.14°C)	0.13°C (0.12°–0.18°C)	0.13°C (0.12°–0.17°C)

approximately 1.8°C per 0.30 COD. Figure 7 depicts a range of cold biases with height varying between 7° and 1°C at 0.30 COD, with the latter corresponding to the altitude where most OTC are present. Where occurrence frequency peaks, near 16.0 km, the simulations suggest bias near 1.8°C.

There is some uncertainty due to MODIS algorithm quality control that may have removed the higher-biased points. First, there is significant SST variance within the sample, despite efforts to constrain it in time and space. The primary mode of points is aggregated near 28°C approaching 0.00 COD, though values range between 24° and 31°C overall. Further, the effects of MODIS QL and data rejection are present at the high COD end of the sample. MODIS NLSST retrieval is partially based on a background/a priori temperature, which is not only often in error by some degree but operationally held below 28°C (Walton et al. 1998). This 28°C background threshold corresponds, interestingly, with the mean, near 0.00 COD, retrieved SST. Furthermore, if the actual and background temperatures are warmer than 28°C, then the retrieved temperature would be nudged toward this 28°C value. There is also the effect of data rejection due to deviation from the background temperature. Because the QL = 1 cutoff nominally occurs at −3°C, it is more likely that climatologically warm pixels will pass quality control when biased by OTC than climatological cool pixels. Thus, the sample shows the effects where lower temperature data points appear cut off at higher COD and lower SST. This effect contributes to the regression slope in opposing ways, where climatologically high SSTs are biased cold due to the cool background when OTC is not present, and climatologically low SSTs are removed due to the deviation test (especially at higher CODs). At any rate, that the effect is distinguishable in these data alone is reasonable.

5. Conclusions

Unscreened cloud contamination within the Level 2 *Aqua*-Moderate Resolution Imaging Spectroradiometer (MODIS) infrared (IR) nonlinear sea surface temperature (NLSST) retrievals at instrument nadir in the tropics (MOD28; 30°S–30°N) during 2012 is characterized

TABLE 3. As in Table 2, but for mean relative (per contaminated observation) cold biases.

Sensor	QL	Global	Atlantic	Indian	Pacific
MODIS	0	0.27°C (0.28°–0.47°C)	0.33°C (0.33°–0.52°C)	0.26°C (0.27°–0.47°C)	0.24°C (0.26°–0.45°C)
	1	0.46°C (0.43°–0.74°C)	0.51°C (0.48°–0.76°C)	0.46°C (0.42°–0.75°C)	0.41°C (0.39°–0.70°C)
	QA	0.33°C (0.33°–0.56°C)	0.40°C (0.39°–0.61°C)	0.32°C (0.32°–0.56°C)	0.30°C (0.30°–0.53°C)
AVHRR	0	0.47°C (0.43°–0.58°C)	0.51°C (0.48°–0.61°C)	0.46°C (0.43°–0.58°C)	0.45°C (0.41°–0.56°C)
	1	0.73°C (0.68°–0.87°C)	0.74°C (0.70°–0.87°C)	0.74°C (0.69°–0.90°C)	0.69°C (0.64°–0.85°C)
	QA	0.55°C (0.52°–0.67°C)	0.60°C (0.56°–0.70°C)	0.55°C (0.51°–0.68°C)	0.53°C (0.49°–0.65°C)
VIIRS	0	0.40°C (0.37°–0.52°C)	0.45°C (0.42°–0.56°C)	0.39°C (0.36°–0.52°C)	0.38°C (0.34°–0.50°C)
	1	0.63°C (0.59°–0.80°C)	0.66°C (0.62°–0.81°C)	0.64°C (0.59°–0.82°C)	0.59°C (0.55°–0.77°C)
	QA	0.48°C (0.44°–0.62°C)	0.53°C (0.49°–0.65°C)	0.47°C (0.43°–0.62°C)	0.45°C (0.41°–0.59°C)

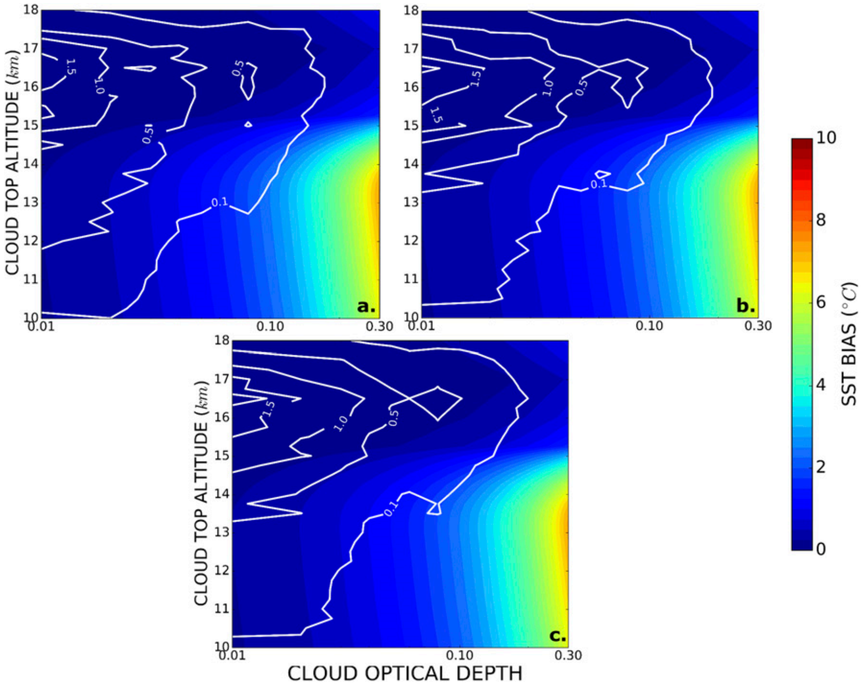

FIG. 8. As in Fig. 7, but for MODIS only over the (a) Atlantic, (b) Indian, and (c) Pacific Ocean basins.

through collocation with Version 3 Level 2 5-km cloud profiles from the Cloud Aerosol lidar with Orthogonal Polarization (CALIOP) instrument. Specifically, optically thin cirrus (OTC; cloud optical depths ≤ 0.30; COD) cloud contamination is highlighted for its predominant contribution to total cloud contamination of IR radiometric retrievals (e.g., Ackerman et al. 2008). Cloud is found present in ~28% of all Level 2 *Aqua*-MODIS data characterized as quality level (QL) = 0 or QL = 1 (denoted as QA), used for quality control dataset characterization, though this may be low given that the specific 5-km cloud product used from CALIOP ignores cloud samples resolved at finer resolutions. Of the contaminating cloud, greater than 90% is cirrus (25.96%). Of this sample, 99.4% is OTC (25.7% absolute), with the remaining clouds being mostly low and warm near-surface liquid water clouds. Such a bimodal residual cirrus/low cloud distribution was also found to contaminate the MODIS aerosol optical depth product (Toth et al. 2013).

OTC contamination characteristics from collocated *Aqua*-MODIS/CALIOP data pairs are used to estimate corresponding IR NLSST retrieval cold biases for MODIS, the Advanced Very High Resolution Radiometer (AVHRR), and the Visible Infrared Imaging Radiometer Suite (VIIRS), as well as triple-window retrievals in AVHRR and VIIRS. Respective SST retrievals are modeled using the Santa Barbara DISORT Atmospheric Radiative Transfer (SBDART) model, equipped with an advanced ice crystal microphysical parameterization and optical scattering properties (Yang et al. 2005; Heymsfield et al. 2014). Two-dimensional OTC-contaminated SST retrieval cold bias matrices are simulated for both the NLSST and triple-window IR algorithms after simulating the retrievals using a tropical standard atmosphere and the presence of a hypothetical OTC layer, 1.5 km thick, between 10.0- and 18.0-km cloud-top height above mean sea level (in 0.25-km segments) and COD between 0.0 and 0.3 (in 0.01 segments from 0.01 to 0.06 and 0.02 segments above 0.06). Simulations are performed using both a cloud structured with a constant optical extinction coefficient (“block cloud”) and one with a linearly decreasing extinction coefficient value from cloud top to cloud base of 5:1 (fallstreak). Having found very little difference in the results, only fallstreak results are presented here. Relative and absolute OTC SST cold biases are then estimated by multiplying the corresponding instrument matrix by the corresponding frequency of OTC occurrence as a function of height and COD estimated from the *Aqua*-MODIS/CALIOP comparisons.

The mean absolute global NLSST OTC SST cold bias estimated across the three platforms from these simulations using a standard atmosphere profile is between 0.09° and 0.14°C using QA *Aqua*-MODIS/CALIOP contamination characteristics, with a corresponding

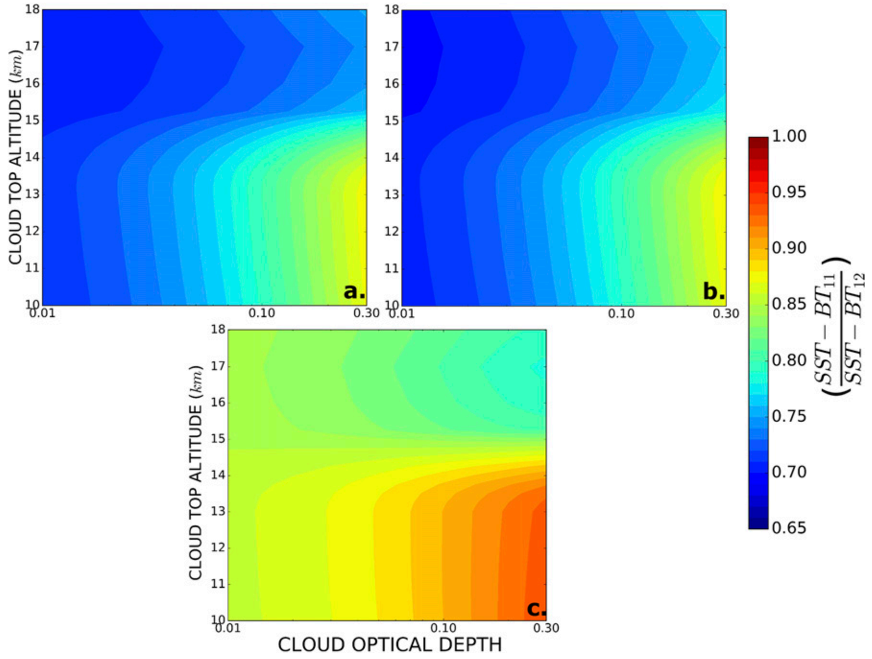

FIG. 9. SBDART radiative transfer model simulations of the ratio of the difference between the true SST and the OTC-contaminated 11- and 12-μm brightness temperatures as a function of cloud-top height and optical depth for (a) AVHRR, (b) MODIS, and (c) VIIRS NLSST algorithms.

global contamination occurrence rate near 25%. The relative bias ranges from 0.33° to 0.55°C. Relative cold biases are higher, reflecting the impact of a single event as opposed to one normalized by its absolute occurrence rates. MODIS exhibits the lowest bias, suggesting increased accuracy due to the more advanced Pathfinder-style NLSST algorithm using different coefficients based on column water vapor. VIIRS corresponds with higher bias, followed closely by AVHRR. After varying the water vapor mixing ratio profile from completely dry (except within the modeled OTC cloud) to liquid water and ice saturated to investigate its impact on the retrieval results, MODIS, AVHRR, and VIIRS vary from 0.09° to 0.14°C, 0.13° to 0.17°C, and 0.11° to 0.16°C absolute, and 0.33° to 0.56°C, 0.52° to 0.67°C, and 0.44° to 0.62°C relative, respectively. In the highest-quality data in MODIS, however, the dry result is higher than the unperturbed result, which requires subsequent reconciliation.

Further examination suggests that the atmospheric correction fails in the presence of cirrus. The NLSST

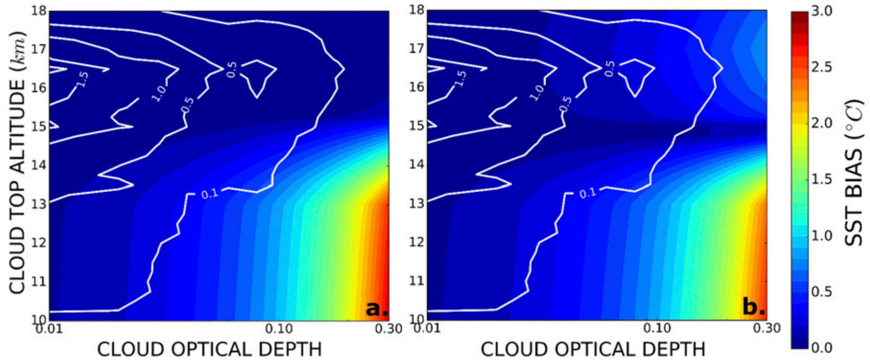

FIG. 10. SBDART radiative transfer model simulations of potential triple-window SST retrieval cold bias for an unscreened OTC as a function of cloud-top height and optical depth for (a) AVHRR and (b) VIIRS. Overlaid on each composite are relative *Aqua*-MODIS/CALIOP collocated cirrus contamination percentage occurrence frequencies (%).

TABLE 4. Mean absolute (relative) OTC cold biases in MODIS, AVHRR, and VIIRS SST triple-window retrievals from SBDART simulations and assuming *Aqua*-MODIS/CALIOP collocated contamination frequencies, segregated as a function of QL, global, and Atlantic, Indian and Pacific Ocean basins.

Sensor	QL	Global	Atlantic	Indian	Pacific
AVHRR	0	0.01°C (0.06°C)	0.01°C (0.08°C)	0.01°C (0.06°C)	0.01°C (0.06°C)
	1	0.04°C (0.11°C)	0.04°C (0.13°C)	0.04°C (0.10°C)	0.04°C (0.10°C)
	QA	0.02°C (0.08°C)	0.02°C (0.10°C)	0.02°C (0.07°C)	0.02°C (0.07°C)
VIIRS	0	0.03°C (0.13°C)	0.02°C (0.13°C)	0.03°C (0.12°C)	0.03°C (0.12°C)
	1	0.07°C (0.19°C)	0.06°C (0.18°C)	0.07°C (0.18°C)	0.07°C (0.18°C)
	QA	0.04°C (0.14°C)	0.03°C (0.15°C)	0.04°C (0.14°C)	0.04°C (0.14°C)

retrieval algorithms are based on the assumption that for constant column water vapor, the difference between the SST and the brightness temperatures from the 11- and 12-μm bands is proportional, such that the atmospheric contribution to measured brightness temperatures can be decoupled from the surface contribution and that an SST retrieval can be performed. Despite the constant column water vapor, the presence of cirrus breaks this proportionality and atmospheric correction fails.

Triple-window simulations show an improved response to OTC presence, though these retrievals are traditionally performed only with reasonable expectation during night due to the high potential for solar contamination of the shortwave IR band used. AVHRR global QA OTC SST bias is estimated at 0.02°C absolute and 0.08°C relative, while VIIRS exhibits slightly lower performance at 0.04°C absolute and 0.14°C relative. The triple-window algorithm is significantly more resilient to OTC presence than NLSST, in spite of its traditionally limited diurnal use.

Both the NLSST and triple-window results are relatively constant across the Indian and Pacific Ocean basins, owing to relatively common cirrus cloud macrophysical properties. Absolute cold biases are lowest over the Atlantic Ocean, corresponding with lower overall cirrus frequency. However, relative cold biases are actually higher in the Atlantic, owing to lower-topped OTC regionally that corresponds with larger cloud-top ice crystal effective radii that act less like water vapor from a spectral standpoint compared with smaller/colder/higher ones elsewhere. This result leads us to conclude that the OTC SST bias is likely to persist significantly while moving away from the tropics, despite lower regional cirrus occurrence frequencies. Consistency in the difference between the clear-sky NLSST and OTC-contaminated brightness temperatures from the near-11- and near-12-μm bands in MODIS, AVHRR, and VIIRS is also presented, depicting the variance in this relationship caused by cloud presence that is symptomatic of the lesser NLSST fidelity.

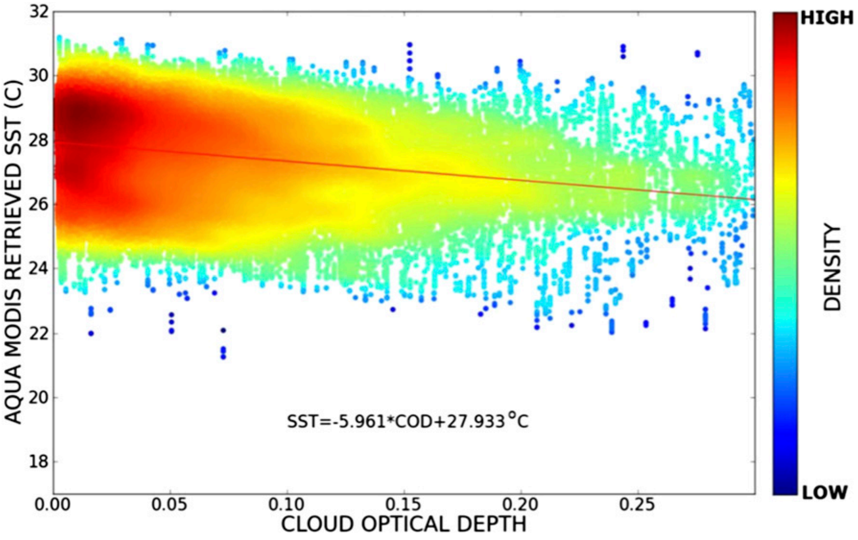

FIG. 11. Scatterplot of CALIOP COD vs *Aqua*-MODIS SST from OTC-contaminated retrievals for August–October 2012 over the Maritime Continent (135°W, 30°N–75°W, 15°S).

Sources of uncertainty relating to these OTC SST cold bias modeling estimates are described. First, cloud contamination characteristics are uniquely extrapolated from *Aqua*-MODIS/CALIOP data pairs to AVHRR and VIIRS. Cold bias estimates for these latter two sensors are thus practical estimates based on this assumption of continuity in OTC contamination between the three IR radiometric sensors. Second, the SBDART simulations are conducted only between 10.0 and 18.0 km. The former coincides with the −37°C level in the standard atmosphere profile used by the model that helps discriminate between cloud tops in the *Aqua*-MODIS/CALIOP collocated dataset and cirrus cloud presence (Campbell et al. 2015). The latter is 1.0 km above the corresponding cold-point tropopause in the standard atmosphere profile, extended slightly to account for the tropical tropopause transition layer (TTL) cirrus cloud presence. In reality, however, OTC cloud-top heights found from the *Aqua*-MODIS/CALIOP data pairs did not all fall within this range (98.93%), meaning that the integrated absolute/relative cold bias estimates are slightly low.

Further uncertainty arises from the use of a static tropical standard atmosphere and static surface SST in deriving the cold bias matrices using the radiative transfer model. Importantly, the *Aqua*-MODIS/CALIOP-contaminated observations are not normalized for height/temperature to the standard atmosphere before integrating the absolute/relative cold bias estimates. Furthermore, the ice particle effective radius is tied to temperature. Subsequent studies may be performed using observations of effective radius from the *CALIPSO* imaging infrared radiometer (IIR) product. The impact of uncertainties in the base CALIOP Level 2 COD product are also described, and the effect is believed negligible given that the accuracy of these values is typically optimal within optically thinner clouds.

Subsequent examination of the impact of using cloud-contaminated data in matchup datasets for the regression of retrieval coefficients is needed. The concern is that roughly a quarter of all best-quality retrievals are contaminated by cloud. When matching these unrealized cloud-contaminated radiances to in situ observations for regression, the coefficients then inadvertently correct for this cloud contamination. The result could be warm-biased true clear-sky retrievals. Furthermore, this study suggests the use of collocated sensor radiances with actively sensed cloud and aerosol profiles for in situ matchups. The use of such a dataset could ensure that no cloud- or aerosol-contaminated radiances are used for regression without correction and thus no clear-sky warm bias.

The community faces a continuing issue with respect to the use of passive remote sensors for operational meteorological and oceanographic measurements: cirrus clouds are the most common cloud genus in the atmosphere, and cloud detection algorithms built off of passive radiances struggle to find OTC that make up roughly half of all of those clouds. With global occurrence rates of 40%–60% (Mace et al. 2009), cirrus—particularly OTC clouds—represent a significant and binding "noise" to passive retrievals that require careful and considerate error characterization for a host of ongoing applications. This paper provides a reasonable and novel set of guidelines for more accurately constraining relative uncertainties in operational SST retrieval products. In the bigger picture, however, as new missions are planned and gradually come online, it is becoming increasingly incumbent upon the scientific community to find practical solutions for suppressing OTC contamination of IR radiometric Level 2 datasets. Whether that means pairing passive satellite sensors with simple/inexpensive lidar profilers, adding of additional infrared bands, or finding advanced spectral analysis methods (e.g., Gao et al. 1998) for improved OTC discrimination, unless the community is willing to deal with an uncertainty that cannot be effectively *seen* passively from space, this problem will continue to persist (e.g., Huang et al. 2016).

Acknowledgments. The authors thank Travis D. Toth for his assistance with constructing the collocation strategies between *Aqua*-MODIS and *CALIPSO*, and for the general advice on the remainder of the experimental design. The authors also thank the anonymous reviewers for their helpful insights. Authors JWM, NJS, and JZ acknowledge the support of NASA Project NNX14AJ13G and NSF Project IIA-1355466. Author JZ also acknowledges the support of ONR N00014-16-1-2040 (Grant 11843919). Author JWM further recognizes the Naval Research Enterprise Internship Program (NREIP), through which he served a 10-week internship at the Naval Research Laboratory during summer 2015, conducting much of this research. Support for his NREIP fellowship came from NASA Interagency Agreement NNG15JA17P on behalf of the Micro-Pulse Lidar Network (E. J. Welton). Authors JRC, JAC and DLW acknowledge the support of Office of Naval Research Code 322 (PE0602435). Author JRC also acknowledges the support of NASA Interagency Agreement RPO201522 on behalf of the *CALIPSO* Science Team (C. R. Trepte).

REFERENCES

Ackerman, S. A., R. E. Holz, R. Frey, E. W. Eloranta, B. C. Maddux, and M. McGill, 2008: Cloud detection with MODIS. Part II: Validation. *J. Atmos. Oceanic Technol.*, **25**, 1073–1086, doi:10.1175/2007JTECHA1053.1.

Barton, I. J., 1995: Satellite-derived sea surface temperatures: Current status. *J. Geophys. Res.*, **100**, 8777–8790, doi:10.1029/95JC00365.

Bogdanoff, A. S., D. L. Westphal, J. R. Campbell, J. A. Cummings, E. J. Hyer, J. S. Reid, and C. A. Clayson, 2015: Sensitivity of infrared sea surface temperature retrievals to the vertical distribution of airborne dust aerosol. *Remote Sens. Environ.*, **159**, 1–13, doi:10.1016/j.rse.2014.12.002.

Brisson, A., P. Le Borgne, and A. Marsouin, 2002: Results of one year of preoperational production of sea surface temperatures from *GOES-8*. *J. Atmos. Oceanic Technol.*, **19**, 1638–1652, doi:10.1175/1520-0426(2002)019<1638:ROOYOP>2.0.CO;2.

Brown, O. B., P. J. Minnett, R. Evans, E. Kearns, K. Kilpatrick, A. Kumar, R. Sikorski, and A. Závody, 1999: MODIS infrared sea surface temperature algorithm. Algorithm Theoretical Basis Doc. Version 2.0, University of Miami, 91 pp.

Campbell, J. R., M. A. Vaughan, M. Oo, R. E. Holz, J. R. Lewis, and E. J. Welton, 2015: Distinguishing cirrus cloud presence in autonomous lidar measurements. *Atmos. Meas. Tech.*, **8**, 435–449, doi:10.5194/amt-8-435-2015.

Chew, B. N., J. R. Campbell, J. S. Reid, D. M. Giles, E. J. Welton, S. V. Salinas, and S. C. Liew, 2011: Tropical cirrus cloud contamination in sun photometer data. *Atmos. Environ.*, **45**, 6724–6731, doi:10.1016/j.atmosenv.2011.08.017.

Davis, G., 2007: History of the NOAA satellite program. *J. Appl. Remote Sens.*, **1**, 012504, doi:10.1117/1.2642347.

Demaria, M., and J. Kaplan, 1994: Sea surface temperature and the maximum intensity of Atlantic tropical cyclones. *J. Climate*, **7**, 1324–1334, doi:10.1175/1520-0442(1994)007<1324:SSTATM>2.0.CO;2.

Deschamps, P. Y., and T. Phulpin, 1980: Atmospheric correction of infrared measurements of sea surface temperature using channels at 3.7, 11 and 12 Mm. *Bound.-Layer Meteor.*, **18**, 131–143, doi:10.1007/BF00121320.

Donlon, C., and Coauthors, 2007: The Global Ocean Data Assimilation Experiment High-Resolution Sea Surface Temperature Pilot Project. *Bull. Amer. Meteor. Soc.*, **88**, 1197–1213, doi:10.1175/BAMS-88-8-1197.

Fueglistaler, S., A. E. Dessler, T. J. Dunkerton, I. Folkins, Q. Fu, and P. W. Mote, 2009: Tropical tropopause layer. *Rev. Geophys.*, **47**, RG1004, doi:10.1029/2008RG000267.

Gao, B.-C., Y. J. Kaufman, W. Han, and W. J. Wiscombe, 1998: Correction of thin cirrus path radiances in the 0.4–1.0 μm spectral region using the sensitive 1.375 μm cirrus detecting channel. *J. Geophys. Res.*, **103**, 32 169–32 176, doi:10.1029/98JD02006.

Garnier, A., J. Pelon, M. A. Vaughan, D. M. Winker, C. R. Trepte, and P. Dubuisson, 2015: Lidar multiple scattering factors inferred from CALIPSO lidar and IIR retrievals of semi-transparent cirrus cloud optical depths over oceans. *Atmos. Meas. Tech.*, **8**, 2759–2774, doi:10.5194/amt-8-2759-2015.

Harris, A., and E. Maturi, 2003: Assimilation of satellite sea surface temperature retrievals. *Bull. Amer. Meteor. Soc.*, **84**, 1575–1580, doi:10.1175/BAMS-84-11-1575.

Heymsfield, A., D. Winker, M. Avery, M. Vaughan, G. Diskin, M. Deng, V. Mitev, and R. Matthey, 2014: Relationships between ice water content and volume extinction coefficient from in situ observations for temperatures from 0° to −86°C: Implications for spaceborne lidar retrievals. *J. Appl. Meteor. Climatol.*, **53**, 479–505, doi:10.1175/JAMC-D-13-087.1.

Hosoda, K., 2011: Algorithm for estimating sea surface temperatures based on Aqua/MODIS global ocean data. 2. Automated quality check process for eliminating cloud contamination. *J. Oceanogr.*, **67**, 791–805, doi:10.1007/s10872-011-0077-5.

Huang, B., C. Liu, V. F. Banzon, H.-M. Zhang, T. R. Karl, J. H. Lawrimore, and R. S. Vose, 2016: Assessing the impact of satellite-based observations in sea surface temperature trends. *Geophys. Res. Lett.*, **43**, 3431–3437, doi:10.1002/2016GL068757.

Huang, J. F., N. C. Hsu, S. C. Tsay, M. J. Jeong, B. N. Holben, T. A. Berkoff, and E. J. Welton, 2011: Susceptibility of aerosol optical thickness retrievals to thin cirrus contamination during the BASE-ASIA campaign. *J. Geophys. Res.*, **116**, D08214, doi:10.1029/2010JD014910.

——, ——, S-C. Tsay, Z. Liu, M.-J. Jeong, R. A. Hansell, and J. Lee, 2013: Use of spaceborne lidar for the evaluation of thin cirrus contamination and screening in the Aqua MODIS Collection 5 aerosol products. *J. Geophys. Res. Atmos.*, **118**, 6444–6453, doi:10.1002/jgrd.50504.

Kelley, J. G. W., D. W. Behringer, H. J. Thiebaux, and B. Balasubramaniyan, 2002: Assimilation of SST data into a real-time coastal ocean forecast system for the U.S. East Coast. *Wea. Forecasting*, **17**, 670–690, doi:10.1175/1520-0434(2002)017<0670:AOSDIA>2.0.CO;2.

Kilpatrick, K. A., G. P. Podestá, and R. Evans, 2001: Overview of the NOAA/NASA advanced very high resolution radiometer Pathfinder algorithm for sea surface temperature and associated matchup database. *J. Geophys. Res.*, **106**, 9179–9197, doi:10.1029/1999JC000065.

Koner, P. K., A. Harris, and E. Maturi, 2015: A physical deterministic inverse method for operational satellite remote sensing: An application for sea surface temperature retrievals. *IEEE Trans. Geosci. Remote Sens.*, **53**, 5872–5888, doi:10.1109/TGRS.2015.2424219.

Lavanant, L., P. Marguinaud, L. Harang, J. Lelay, S. Péré, and S. Phillippe, 2007: Operational cloud masking for the OSI SAF global METOP/AVHRR SST product. *Proc. Joint 2007 EUMETSAT Meteorological Satellite Conf. and the 15th Satellite Meteorology and Oceanography Conf. of the American Meteorological Society*, Amsterdam, Netherlands, EUMETSAT and Amer. Meteor. Soc., 259, 8 pp. [Available online at http://www.eumetsat.int/website/wcm/idc/idcplg?IdcService=GET_FILE&dDocName=PDF_CONF_P50_S8_07_LAVANANT_P&RevisionSelectionMethod=LatestReleased&Rendition=Web.]

Le Borgne, P., G. Legendre, and A. Marsouin, 2007: Operational SST retrieval from METOP/AVHRR. *Proc. Joint 2007 EUMETSAT Meteorological Satellite Conf. and the 15th Satellite Meteorology and Oceanography Conf. of the American Meteorological Society*, Amsterdam, Netherlands, EUMETSAT and Amer. Meteor. Soc., 10 pp. [Available online at http://www.eumetsat.int/website/wcm/idc/idcplg?IdcService=GET_FILE&dDocName=PDF_CONF_P50_S5_01_LEBORGNE_V&RevisionSelectionMethod=LatestReleased&Rendition=Web.]

Llewellyn-Jones, D. T., P. J. Minnett, R. W. Saunders, and A. M. Zavody, 1984: Satellite multichannel infrared measurements of sea surface temperature of the N.E. Atlantic Ocean using AVHRR/2. *Quart. J. Roy. Meteor. Soc.*, **110**, 613–631, doi:10.1002/qj.49711046504.

Mace, G. G., Q. Zhang, M. Vaughan, R. Marchand, G. Stephens, C. Trepte, and D. Winker, 2009: A description of hydrometeor layer occurrence statistics derived from the first year of merged Cloudsat and CALIPSO data. *J. Geophys. Res.*, **114**, D00A26, doi:10.1029/2007JD009755.

McClain, E. P., W. G. Pichel, and C. C. Walton, 1985: Comparative performance of AVHRR-based multichannel sea surface temperatures. *J. Geophys. Res.*, **90**, 11 587–11 601, doi:10.1029/JC090iC06p11587.

Merchant, C. J., and P. Le Borgne, 2004: Retrieval of sea surface temperature from space, based on modeling of infrared radiative transfer: Capabilities and limitations. *J. Atmos. Oceanic Technol.*, **21**, 1734–1746, doi:10.1175/JTECH1667.1.

——, A. R. Harris, M. J. Murray, and A. M. Závody, 1999: Toward the elimination of bias in satellite retrievals of sea surface temperature: 1. Theory, modeling and interalgorithm comparison. *J. Geophys. Res.*, **104**, 23 565–23 578, doi:10.1029/1999JC900105.

——, P. Le Borgne, A. Marosuin, and H. Roquet, 2008: Optimal estimation of sea surface temperature from split-window observations. *Remote Sens. Environ.*, **112**, 2469–2484, doi:10.1016/j.rse.2007.11.011.

——, A. R. Harris, E. Maturi, O. Embury, S. N. MacCallum, J. Mittaz, and C. P. Old, 2009: Sea surface temperature estimation from the *Geostationary Operational Environmental Satellite-12* (*GOES-12*). *J. Atmos. Oceanic Technol.*, **26**, 570–581, doi:10.1175/2008JTECHO596.1.

——, and Coauthors, 2012: A 20 year independent record of sea surface temperature for climate from Along Track Scanning Radiometers. *J. Geophys. Res.*, **117**, C12013, doi:10.1029/2012JC008400.

Miller, B. I., 1958: On the maximum intensity of hurricanes. *J. Meteor.*, **15**, 184–195, doi:10.1175/1520-0469(1958)015<0184:OTMIOH>2.0.CO;2.

Minnett, P. J., and Coauthors, 2013: Assessment of Suomi-NPP VIIRS sea surface temperature retrievals. University of Miami, 26 pp.

Miyazawa, Y., H. Murakami, T. Miyama, S. M. Varlamov, X. Guo, T. Waseda, and S. Sil, 2013: Data assimilation of the high-resolution sea surface temperature obtained from the Aqua-Terra satellites (MODIS-SST) using an ensemble Kalman filter. *Remote Sens.*, **5**, 3123–3139, doi:10.3390/rs5063123.

Petrenko, B., A. Ignatov, Y. Kihai, J. Stroup, and P. Dash, 2014: Evaluation and selection of SST regression algorithms for JPSS VIIRS. *J. Geophys. Res. Atmos.*, **119**, 4580–4599, doi:10.1002/2013JD020637.

Pichel, W., E. Maturi, P. Clemente-Colón, and J. Sapper, 2001: Deriving the operational nonlinear multichannel sea surface temperature algorithm coefficients for NOAA-15 AVHRR/3. *Int. J. Remote Sens.*, **22**, 699–704, doi:10.1080/014311600010013793.

Reynolds, R. W., and T. M. Smith, 1994: Improved global sea surface temperature analyses using optimum interpolation. *J. Climate*, **7**, 929–948, doi:10.1175/1520-0442(1994)007<0929:IGSSTA>2.0.CO;2.

Ricchiazzi, P., S. Yang, C. Gautier, and D. Sowle, 1998: SBDART: A research and teaching software tool for plane-parallel radiative transfer in the Earth's atmosphere. *Bull. Amer. Meteor. Soc.*, **79**, 2101–2114, doi:10.1175/1520-0477(1998)079<2101:SARATS>2.0.CO;2.

Roemmich, D., and Coauthors, 2009: The Argo program: Observing the global ocean with profiling floats. *Oceanography*, **22**, 34–43, doi:10.5670/oceanog.2009.36.

Sassen, K., and B. S. Cho, 1992: Subvisual-thin cirrus lidar dataset for satellite verification and climatological research. *J. Appl. Meteor.*, **31**, 1275–1285, doi:10.1175/1520-0450(1992)031<1275:STCLDF>2.0.CO;2.

——, Z. Wang, and D. Liu, 2008: Global distribution of cirrus clouds from CloudSat/Cloud Aerosol Lidar and Infrared Pathfinder Satellite Observations (CALIPSO) measurements. *J. Geophys. Res.*, **113**, D00A12, doi:10.1029/2008JD009972.

Stephens, G. L., and Coauthors, 2002: The CloudSat mission and the A-Train: A new dimension of space-based observations of clouds and precipitation. *Bull. Amer. Meteor. Soc.*, **83**, 1771–1790, doi:10.1175/BAMS-83-12-1771.

Sun, Z., and K. P. Shine, 1994: Studies of the radiative properties of ice and mixed-phase clouds. *Quart. J. Roy. Meteor. Soc.*, **120**, 111–137, doi:10.1002/qj.49712051508.

Tang, Y., R. Kleeman, and A. M. Moore, 2004: SST assimilation experiments in a tropical Pacific Ocean model. *J. Phys. Oceanogr.*, **34**, 623–642, doi:10.1175/3518.1.

Toth, T. D., and Coauthors, 2013: Investigating enhanced Aqua MODIS aerosol optical depth retrievals over the mid-to-high latitude Southern Oceans through intercomparison with co-located CALIOP, MAN, and AERONET data sets. *J. Geophys. Res. Atmos.*, **118**, 4700–4714, doi:10.1002/jgrd.50311.

Vaughan, M. A., and Coauthors, 2009: Fully automated detection of cloud and aerosol layers in the CALIPSO lidar measurements. *J. Atmos. Oceanic Technol.*, **26**, 2034–2050, doi:10.1175/2009JTECHA1228.1.

Vázquez-Cuervo, J., E. M. Armstrong, and A. Harris, 2004: The effect of aerosols and clouds on the retrieval of infrared sea surface temperatures. *J. Climate*, **17**, 3921–3933, doi:10.1175/1520-0442(2004)017<3921:TEOAAC>2.0.CO;2.

Walton, C. C., 1988: Nonlinear multichannel algorithms for estimating sea surface temperature with AVHRR satellite data. *J. Appl. Meteor.*, **27**, 115–124, doi:10.1175/1520-0450(1988)027<0115:NMAFES>2.0.CO;2.

——, W. G. Pichel, J. F. Sapper, and D. A. May, 1998: The development and operational application of nonlinear algorithms for the measurement of sea surface temperatures with cthe NOAA polar-orbiting environmental satellites. *J. Geophys. Res.*, **103**, 27 999–28 012, doi:10.1029/98JC02370.

Winker, D. M., M. A. Vaughan, A. Omar, Y. Hu, K. A. Powell, Z. Liu, W. H. Hunt, and S. A. Young, 2009: Overview of the CALIPSO mission and CALIOP data processing algorithms. *J. Atmos. Oceanic Technol.*, **26**, 2310–2323, doi:10.1175/2009JTECHA1281.1.

——, and Coauthors, 2010: The CALIPSO mission: A global 3D view of aerosols and clouds. *Bull. Amer. Meteor. Soc.*, **91**, 1211–1229, doi:10.1175/2010BAMS3009.1.

Wu, X., W. P. Menzel, and G. S. Wade, 1999: Estimation of sea surface temperatures using *GOES-8/9* radiance measurements. *Bull. Amer. Meteor. Soc.*, **80**, 1127–1138, doi:10.1175/1520-0477(1999)080<1127:EOSSTU>2.0.CO;2.

Yang, P., H. Wei, H.-L. Huang, B. A. Baum, Y. X. Hu, G. W. Kattawar, M. I. Mishchenko, and Q. Fu, 2005: Scattering and absorption property database for nonspherical ice particles in the near- through far-infrared spectral region. *Appl. Opt.*, **44**, 5512–5523, doi:10.1364/AO.44.005512.

Young, S. A., and M. A. Vaughan, 2009: The retrieval of profiles of particulate extinction from Cloud-Aerosol Lidar Infrared Pathfinder Satellite Observations (CALIPSO) data: Algorithm description. *J. Atmos. Oceanic Technol.*, **26**, 1105–1119, doi:10.1175/2008JTECHA1221.1.